Multidimensional multiphoton momentum microscopy of the anisotropic Ag(110) surface

Andi Li [1], Marcel Reutzel [1,2], Zehua Wang,[1] David Schmitt,[2] Marius Keunecke,[2] Wiebke Bennecke,[2]
G. S. Matthijs Jansen [2], Daniel Steil [2], Sabine Steil,[2] Dino Novko [3,4], Branko Gumhalter [3],
Stefan Mathias [2,5] and Hrvoje Petek [1,*]

[1]*Department of Physics and Astronomy and Pittsburgh Quantum Institute, University of Pittsburgh, Pittsburgh, Pennsylvania, USA*
[2]*I. Physikalisches Institut, Georg-August-Universität Göttingen, Göttingen, Germany*
[3]*Institute of Physics, Zagreb, Croatia*
[4]*Donostia International Physics Center (DIPC), San Sebastián, Spain*
[5]*International Center for Advanced Studies of Energy Conversion (ICASEC), University of Göttingen, Göttingen, Germany*

We investigate the strongly anisotropic near-surface electronic band structure of Ag(110) by multidimensional momentum microscopy within the energy-momentum space of the Brillouin zone accessible to multiphoton photoemission (mPP). The momentum imaging of the near-surface band structure reveals an unexpected plethora of energy-momentum mPP features arising from surface-surface, surface-bulk, and bulk-bulk optical transitions. The nonlinear excitation enables the imaging of the surface and bulk bands over a wider energy-momentum range than is available to linear photoemission spectroscopy. The mPP spectra record the unusual in-surface-plane responses involving resonances with the known Shockley surface states of Ag(110) at the $\bar{Y}$ point, as well as the strongly anisotropic surface state in a minigap at the $\bar{\Gamma}$ point, which mediates the plasmonic photoemission of Ag(110). In addition, image potential surface states and resonances of Ag(110) appear with different contrast that is defined by their parallel momentum-dependent projections onto the projected bands and gaps, the resonance conditions from the lower surface and bulk bands, as well as the order of the nonlinear photoemission process.

I. INTRODUCTION

High electron density metals are model systems for studying electronic band structures, many-body screening effects, and linear and nonlinear light-matter interactions [1–5]. Upon chemisorption of atoms or molecules, metals acquire even more complex properties leading to, for example, interfacial charge transfer, thermionic and photoelectric emission, and catalysis [6–8]. The understanding and design of such properties enables contributions to science and technology, for example, via plasmonic chemistry or solar energy harvesting [8–10]. Thus, a thorough understanding of the electronic structure of pristine, atomically defined metal surfaces is a prerequisite for exploring and manipulating their electronic and dynamical properties.

The high-symmetry (111) and (100) crystal planes of noble metals (copper, silver, and gold) have been studied extensively with optical and photoemission spectroscopic techniques [11–26] including momentum microscopy [27–31]. By contrast, the (110) surfaces have hardly been spectroscopically investigated [32] even though they are employed as substrates for atomic or molecular orbital alignment, imaging, nanostructure growth, and photocatalysis [33–37]. Their large structural and electronic anisotropy differentiates them from the more familiar (111) and (100) counterparts, by exhibiting strongly polarization- and alignment-dependent linear [38–40] and nonlinear optical responses [41]. Polarized

absorption/reflection spectroscopy in the 2–5 eV spectral range has revealed anisotropic single particle intra- and interband responses [38–40], while the intense bulk plasmon at 3.8–3.9 eV also participates in the plasmonic excitation and photoemission response [42–45].

The electronic band structure of Ag(110) within several electronvolts from the Fermi level (E_F) has also been investigated by conventional photoemission (1PP), inverse photoemission (IPE), surface second harmonic generation (SSHG) spectroscopy, and scanning tunneling microscopy (STM); its known electronic properties will be summarized in Sec. II [41,46–50]. However, a recent study of the plasmonic photoemission response of single-crystal Ag surfaces [43–45] revealed that the (110) surface exhibits remarkably rich and unexpected single-particle and collective response features that invite further examination [51].

Previously, Sonoda [52] investigated the electronic structure of the related Cu(110) surface by two-photon photoemission (2PP) spectroscopy with variously polarized tunable ultraviolet (UV) excitation light. He found surprisingly rich angle-resolved spectra involving excitations from surface and bulk d bands as the initial states to the unoccupied sp-band intermediate and final states in the $\bar{Y}\bar{\Gamma}\bar{X}$ momentum directions. Tsirkin *et al.* [53] and Tsirkin and Chulkov [54] have parametrized the anisotropic two-dimensional (2D) electronic band structures of both the Ag(110) and Cu(110) surfaces, and Eremeev *et al.* [55], Tsirkin *et al.* [56], and Sklyadneva *et al.* [57] calculated their electron-phonon interactions. Li *et al.* [44] and Novko *et al.* [45] performed detailed density functional theory (DFT)-based calculations of the Ag(110)
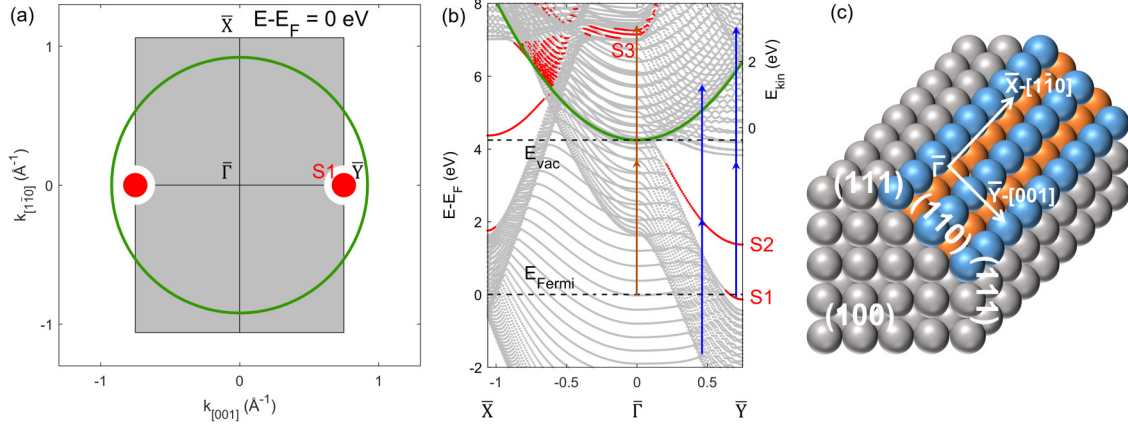
*petek@pitt.edu

FIG. 1. Electronic structure of Ag(110) and accessible in-plane momentum range within two-photon photoemission (2PP) spectroscopy. (a) Two-dimensional (2D) cut through the surface projected Brillouin zone of Ag(110) at the Fermi energy; the gray region represents surface projected occupied bulk bands of the first Brillouin zone. At the $\bar{Y}$ point, the S1$^{(occ)}$ state (red circles) is found in the surface projected bandgap (white semicircle). The green circle depicts the photoelectron horizon, i.e., the maximum accessible in-plane momentum at Fermi level excited with two 3.72 eV photons. (b) Surface projected band structure of Ag(110). Gray and red colors represent bands with bulk and surface character, respectively. Blue arrows indicate excitation of S1$^{(occ)}$ and S2 states with 3.72 eV photons. Brown arrows indicate plasmonic photoemission pathways terminating in the surface state S3. Only excitations above the photoemission horizon (green parabola) can be measured. (c) The atomic structure of Ag(110) surface formed at a junction of two (111) surfaces. The blue (high) and orange (low) balls emphasize the ridges and troughs of the anisotropic (110) surface.

surface electronic band structure and found evidence for a previously unknown surface band lying in a highly anisotropic minigap at the $\bar{\Gamma}$ point, which acts as a final state in the plasmonic 2PP with >3.7 eV light.

Motivated by the appearance of unexpected single-particle spectroscopic features in a 2PP and four-photon photoemission (4PP) study of plasmonic photoemission of the Ag(110) surface [51], we examine in detail the three-dimensional (3D) energy-momentum bands via multiphoton photoemission (mPP, $m \geqslant 2$; photon energy $\hbar\omega = 1.5$–4.2 eV). To this end, we exploit the 3D photoelectron imaging capabilities of a time-of-flight momentum microscope [58,59]. These measurements are augmented by 2D energy-momentum mPP spectroscopy with a hemispherical electron energy analyzer. The measurements probe the single-particle and collective nonlinear responses of the Ag(110) surface pertaining to the surface electronic structure, surface photochemistry, and plasmonic photoemission [36,44,51,60,61].

II. STRUCTURAL AND ELECTRONICAL PROPERTIES OF Ag(110)

Before embarking on the experimental results, we introduce the key aspects of atomic and electronic structure of the Ag(110) surface which define its electronic response to optical fields. The well-known Ag(111) and Ag(100) surfaces have inverted sp-projected bandgaps centered at the $\bar{\Gamma}$ point that separate the nearly free electron conduction bands from Mahan cones derived from them by translation in reciprocal lattice vectors $\vec{G}$ [62]. Such bandgaps support surface states that penetrate evanescently into the bulk and consequently have relatively long phase and energy relaxation times [2,24,63–67]. The Ag(110) surface occurs at junctions of (111) and (100) surfaces, where their corresponding bandgaps project in the off-normal L and X directions. This construction

from pairs of proximate crystallographic planes defines the electronic anisotropy of the (110) surface, as illustrated in Figs. 1(a) and 1(b). Moreover, the sp band of the Ag(110) surface disperses in the bulk Γ-K direction without opening an evident gap at the $\bar{\Gamma}$ point. Therefore, the image potential and other surface states become broad resonances at energies and parallel momenta where they are degenerate with the bulk sp band. The wave functions of such surface resonances propagate into the bulk, and hence, their decay rates are enhanced with respect to the evanescent surface states [2,66,68]. Consequently, they do not participate as bright intermediate states in 2PP spectra, as do surface states within the bandgaps on other surfaces [68]. This anticipated lack of sharp surface state structure at the $\bar{\Gamma}$ point has discouraged the studies of unoccupied surface electronic structure of the Ag(110) surface. The only historical 2PP study of the Ag(110) surface at the $\bar{\Gamma}$ point reported the hot electron lifetimes for excitation below the interband threshold of 3.87 eV [69] involving primarily the intraband Drude absorption [70]. No 2PP study of the Ag(110) electronic structure has been reported except for our preliminary report of plasmonic and above threshold mPP [44,51], which stimulate this more comprehensive investigation.

Specifically, our study is motivated by the discovery of plasmonic photoemission on low-index single-crystal Ag surfaces, including the (110) facet [44]. When the photoexcitation energy is tuned to or above $\hbar\omega \gtrsim 3.7$–3.9 eV, corresponding to the bulk longitudinal plasmon frequency, which coincides with the dielectric function of Ag passing through zero, the local collective plasmon field excites electrons preferentially from E_F [43,44], contrary to the common belief and theory that the plasmon excitation decays into hot holes in an energy range of $-\hbar\omega$ to E_F and hot electrons in the range of E_F to $+\hbar\omega$ [71,72]. Under intense laser excitation, we discovered that the plasmonic photoemission at low-index silver surfaces occurs nonlinearly by annihilation of two bulk

plasmon quanta promoting photoelectrons specifically from E_F, as evidenced by peaklike features in 2PP spectra [44,73]. In the case of the Ag(110) surface, we attributed this particular plasmonic photoemission feature to 2PP excitation of electrons from E_F to a final surface state at an energy of $E\text{-}E_F \sim 7.6\,\text{eV}$, which we discovered to be highly anisotropic and centered at the $\bar{\Gamma}$ point within a previously unknown minigap in the sp band. The density functional electronic structure theory [45] predicts such a state at $E\text{-}E_F \sim 7.14\,\text{eV}$ within a minigap spanning the interval of 7.0–7.3 eV [S3 in Fig. 1(b)].

The (110) surface is formed by slicing the apex of a junction between two proximate (111) surfaces of a face-centered cubic (fcc) lattice. The surface structure, as depicted in Fig. 1(c), is serrated, consisting of close-packed rows of atoms that belong to the two joining (111) planes and propagate in the $\overline{\Gamma X}$ or the $[1\bar{1}0]$ direction. Each contributing (111) surface is two atoms wide, forming serried upper ridge and lower trough atomic layer corrugation of the (110) surface. The corrugation of these ridge-and-trough close-packed atomic rows runs in the $\overline{\Gamma Y}$ or the [001] direction [56]. The two (111) plane junctions support two Shockley surface states within a bandgap that extends from -0.4 to 3.8 eV like the one on the (111) surface but with band minima at the $\bar{Y}$ point [right part of Fig. 1(b) where the surface states are colored red]. The lower energy one is the partially occupied surface state (S1) with its band minimum at 0.1 eV below E_F and a nearly isotropic band mass of $0.26\,m_e$ [46], which has similar characteristics to that of the (111) plane and is localized predominantly within the corrugation troughs [56]. The upper one is an unoccupied surface state (S2) running on top of the Ag atom ridges [56] and with a band minimum at ~ 1.7 eV above E_F and mass of $\sim 0.7\,m_e$ [48].

The surface states at the $\bar{Y}$ point have been investigated by 1PP, IPE, and mPP [46,47,50,51]. They also resonantly enhance the SSHG signal and can be imaged as tunneling resonances in STM [41,48,74]. The S2 $\leftarrow$ S1 transition, which is one-photon resonant for $\hbar\omega \sim 1.7$ eV, enhances the nonlinear SSHG as well as 4PP spectra [41,51]. An unusual aspect of this transition is that it is excited by the in-plane optical field polarized in the [001] crystalline direction. Although the surface parallel optical fields must nominally pass through zero in the near-surface region [1], the spatial separation of S2 and S1 at single-atom-high ridges and troughs on the Ag(110) surface [56] requires their coupling by in-plane surface fields that are orthogonal to the serration (along the $\overline{\Gamma Y}$ direction) [41,44]. This optical transition thus entails charge transduction both normal and parallel to the surface. A possibly related optical response occurring $\geqslant 3.7$–3.8 eV is the excitation of the bulk longitudinal plasmon mode of Ag(110) when the s-polarized optical field is polarized in the [001] direction, which is highly unexpected because surface parallel fields usually do not provide momentum to couple into the plasmon mode. Nevertheless, s-polarized optical fields (in the [001] direction) drive the surface parallel and normal charges, enabling the excitation of the bulk plasmon response [1,44].

In the less investigated orthogonal $[1\bar{1}0]$ direction, according to our DFT-based calculation, the $\bar{X}$-point bandgap extends from 1.6 to 7.0 eV above E_F and hosts two surface states at 1.8 and 4.4 eV [44]. While the latter has been confirmed in the IPE spectra [47], the former has not been

reported. These are some of the established but in many respects uncommon features of the Ag(110) surface that relate to its exceptional mPP spectra. Other mPP spectral features can be attributed to the bulk bands, as will be explained further below.

III. METHODS

A. Experiments

The mPP spectroscopy is performed in two photoemission apparatus that offer distinct advantages. To characterize the electronic anisotropy of Ag(110), a time-of-flight momentum microscope records 3D energy vs in-plane $k_{[1\bar{1}0]}$ and $k_{[001]}$ parallel momenta 2PP spectral distributions of photoemitted electrons excited by ultrashort UV pulses [59]. We supplement this data with three-photon photoemission (3PP) and 4PP measurements of 2D energy-momentum photoelectron distributions acquired by a hemispherical electron energy analyzer with a more restricted energy-momentum window following visible-infrared excitation. These higher nonlinear order measurements aid in confirming the momentum microscope assignments by recording the same electronic bands with higher sensitivity, including the above threshold photoemission [24,25,75].

The two-photon momentum microscopy experiments [58,76] are performed at the University of Göttingen with a METIS, Surface Concept GmbH instrument [29,59]. The 2PP excitation is performed with an optical parametric amplifier (OPA; Orpheus-F/HP, Light Conversion) that is pumped by an AFS Fiber laser system operating at 0.5 MHz repetition rate. The OPA output is frequency doubled to $\hbar\omega = 3.43$–3.86 eV to excite 2PP with p-polarized, ~ 40 fs light pulses. The light pulses are directed onto the sample at an angle of incidence of $68°$ from the surface normal; the $\overline{\Gamma Y}$ direction of the Ag(110) crystal is aligned to be in the optical plane. Within the momentum microscope, an extractor voltage of 10 kV is applied to enable recording of photoemission momentum distributions within a solid angle of 2π centered on the surface normal to capture the full photoemission horizon [58,59]. The energy- and momentum-axes are calibrated as explained in Ref. [59].

In addition, we measure mPP spectra with a hemispherical electron energy analyzer with an angular acceptance angle of $\sim \pm 13°$ (PHOIBOS, Specs GmbH) and a 2D delay line electron counting detector (Surface Concept GmbH) at the University of Pittsburgh [16,24,51]. Unless stated otherwise, the 3PP and 4PP 2D photoelectron energy vs parallel momentum spectra are taken with the Ag(110) surface aligned with the $\overline{\Gamma Y}$ direction in the optical plane. The excitation light is generated with two noncollinear OPA lines, which are pumped by the second and third harmonics of a Yb-doped fiber laser oscillator-amplifier system (Impulse, Clark MXR). The excitation is performed with p-polarized light incident at $45°$ with respect to the analyzer optical axis in the 930–550 nm (1.3–2.3 eV) range with 20–30 fs duration pulses operating at 1 MHz repetition rate. In the experiments focusing on the image potential state series of Ag(110), the photoelectron spectra are detected close to normal emission. To reach additional features centered at the $\bar{Y}$ point, we rotate the sample around the axis normal to the optical plane. In this configuration, the laser optical field becomes effectively
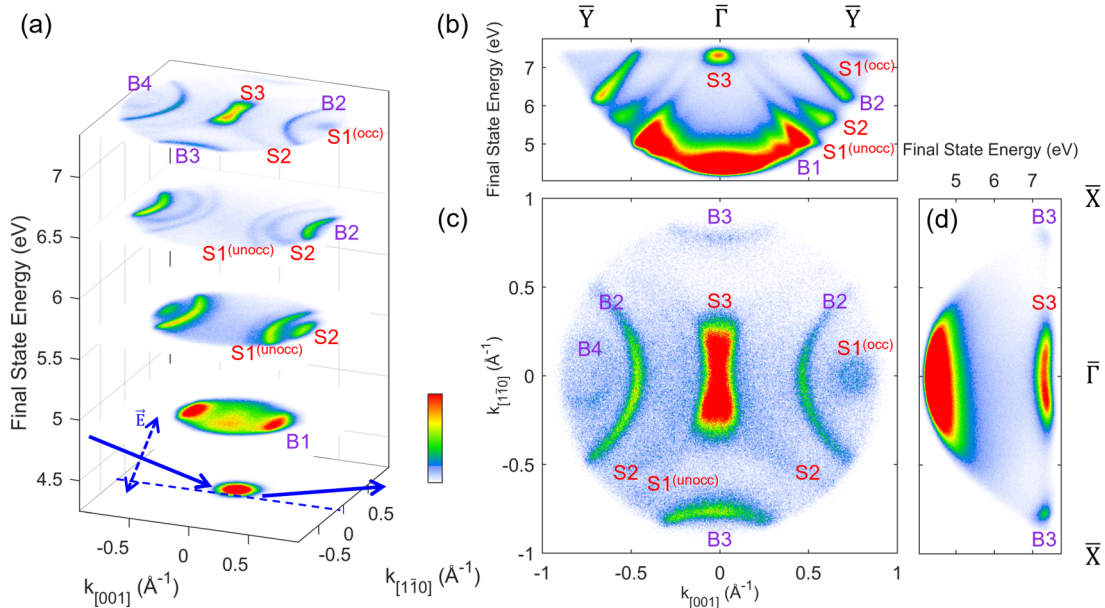
FIG. 2. Two-photon photoemission momentum microscopy of Ag(110) with *p*-polarized $\hbar\omega = 3.72$ eV light. (a) Three-dimensional (3D) data stack illustrating the photoemission yield (color coded) as a function of energy (bottom to top slices are cut at 4.25, 4.85, 5.65, 6.5, and 7.35 eV final state energy) and in-plane ($k_{\parallel}$) momenta. The entire 3D spectrum of Ag(110) is displayed as a movie in the Supplemental Material [80]. Solid blue arrows indicate laser propagation direction, and dashed blue arrow indicates electric field direction of *p*-polarized light. (b) $E_f(k_{[001]})$-resolved spectra cut at $k_{[1\bar{1}0]} = 0 \pm 0.07$ Å^{-1} window. (c) $(k_{[001]}, k_{[1\bar{1}0]})$-resolved spectra cut at $E_F + 2\hbar\omega$, or $E_f = 7.44 \pm 0.04$ eV window. (d) $E_f(k_{[1\bar{1}0]})$-resolved spectra cut at $k_{[001]} = 0 \pm 0.07$ Å^{-1} window. Purple and red text labels indicate transitions assigned to specific bulk and surface states, respectively.

parallel to the surface. As explained in Sec. II, this geometry drives mPP excitations with exceptional transition moments in the surface plane [41,44,51].

Both photoemission experiments are performed in ultra-high vacuum chambers having base pressures of $<10^{-10}$ mbar. The pristine Ag(110) surface is prepared from the same sample by multiple cycles of Ar$^+$ ion sputtering (1500 V, 3 μA, 20 min) and subsequent annealing (550 K, 10 min). The surface quality is confirmed by the work function energy of $\Phi \sim 4.25$ eV as well as sharp and intense surface state mPP signals at the $\bar{Y}$ point [51].

B. Theoretical calculations

The surface and bulk band structures of Ag(110) are calculated by the QUANTUM ESPRESSO DFT plane-wave code [77]. Norm-conserving Vanderbilt pseudopotentials are used with the PBE exchange-correlation functional [78,79]. To correctly calculate the energy positions of the *d* bands, the Hubbard onsite interaction of $U = 3.1$ eV is applied.

The Ag(110) surface band structure is obtained from a 51-layer slab calculation by using a supercell approach and a plane-wave cutoff energy of 80 Ry. The slabs in the adjacent supercells are separated by vertical vacuum, large enough to ensure negligible interactions between them. A $6 \times 6 \times 1$ Monkhorst-Pack grid is utilized for sampling the Ag(110) Brillouin zone, with Gaussian smearing of 0.01 Ry. The unit cell dimension of $a = 4.06$ Å is adopted. The calculation describes the electronic structures of both the Ag(110) surface and bulk continua.

A calculation of the pure bulk band structure of 3D fcc Ag is also performed. For this purpose, a $20 \times 20 \times 20$ Monkhorst-Pack grid samples the Brillouin zone. The pure bulk band contributions to the Ag(110) electronic structure are obtained by projecting the different $k_\perp$ states onto the (110) surface plane with the surface normal momentum conservation relaxed. These calculations allow consideration of how the bulk band structure of Ag(110) is accessed at the (110) surface plane. Note, however, that this method does not predict the surface states on the Ag(110) surface because the vacuum interface does not exist.

IV. RESULTS

A. Overview of the photoemission data

Figure 2 shows the 2PP momentum microscopy data collected from the pristine Ag(110) surface with *p*-polarized, $\hbar\omega = 3.72$ eV excitation. The momentum microscope collects the entire photoelectron distribution for energies and momenta above the photoemission horizon, as is directly evident in the data from the parabolic cutoff photoemission signals at low-energy boundaries in Figs. 2(b) and 2(d); below this threshold, no momentum conserving photoemission occurs [51]. The 3D spectrum is plotted in Fig. 2(a) for selected energy slices with respect to the measured final state energy E_F relative to E_F for all the in-plane momenta ($k_{[1\bar{1}0]}$ and $k_{[001]}$ directions are indicated) above the photoemission horizon. The full 3D dataset covering $E_f = 4.2$–7.8 eV is available as a movie in the Supplemental Material [80]. In Figs. 2(b) and 2(d), the 3D data are presented as 2D cross-sections for fixed $k_{[1\bar{1}0]} = 0$ Å^{-1}
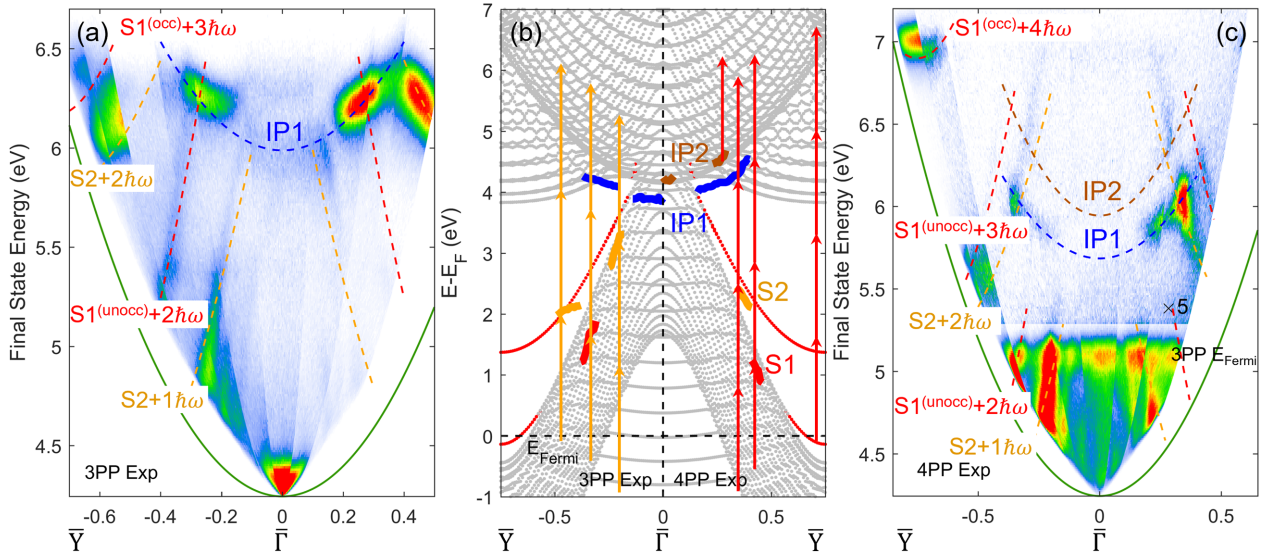
FIG. 3. $E_f(k_{[001]})$-resolved 3PP and 4PP spectra of Ag(110) excited with (a) $\hbar\omega = 2.09$ eV light; and (c) $\hbar\omega = 1.72$ eV light. Surface state dispersions in (a) and (c) are extracted and plotted in the left and right part of (b) that contains the calculated Ag(110) surface and bulk band structure in $\overline{\Gamma Y}$ direction. Specific assignments are indicated in the figure, where red and orange dashed lines represent excitations from the S1 and S2 states, respectively. Green solid lines in (a) and (c) represent photoemission horizon. Discontinuous jumps in the mPP intensity [(a) and (c)] are caused by the assembly of spectra from multiple $E_f(k_{[001]})$-measurements for different sample angles with respect to the electron energy analyzer entrance axis. The signal below 5.16 eV in (c) is from 3PP and above from 4PP excitation (amplified by five times).

and $k_{[001]} = 0$ Å^{-1}, respectively. The recorded signals in both 2D sections terminate above the $E_f = 2\hbar\omega + E_F$ [Fig. 2(c)] energy slice.

In normal emission, the accessible E_f range of the 2PP measurements with $\hbar\omega = 3.72$ eV light is limited by the work function of Ag(110) of $\Phi \sim 4.25$ eV on the low end and ~ 7.4 eV by two-photon plasmonic photoemission of electrons from the Fermi level at the high end [44]. In addition to the plasmonically excited anisotropic final state surface band S3, the spectra in Figs. 2(b) and 2(d) show evidence of seven transitions involving strongly dispersive bands that extend over the entire accessible Brillouin zone. The existence of such bands has already been noted in Ref. [51], but they have not been assigned. As we will show, four of these features (B1–B4) involve transitions between the bulk sp bands of Ag(110), whereas the remaining ones are assigned to S1 and S2 surface state excitations, in some cases involving optical transitions from or to the bulk bands in the mPP process. The bulk bands that optically couple to surface states must have a large spatial overlap with the latter.

To further define spectral assignments of these transitions, we increase the nonlinear order of photoemission process by tuning the photon energies between $\hbar\omega = 1.72$ and 2.09 eV. These excitations in the visible region cannot excite one-photon momentum conserving bulk interband transitions in silver. Instead, the high fluences available from ultrafast lasers can excite interband transitions in higher order 3PP and 4PP processes [25]. The mPP data at these photon energies are shown in Figs. 3(a) and 3(c), and the extracted peak dispersions are plotted in the band structure as thick colored solid lines in the left (3PP) and right (4PP) parts of Fig. 3(b). In addition, in Figs. 3(a) and 3(c), red and orange dashed parabolas, representing S1 and S2 states, respectively, are plotted using

the parameters extracted from the 2PP momentum microscopy data; they are plotted at the 3PP and 4PP final state energy E_f positions, showing a good agreement in band dispersions between data obtained from photoemission processes of different nonlinearities.

Furthermore, in 3PP and 4PP, we detect spectral densities belonging to the image potential state series ($n = 1$: IP1, $n = 2$: IP2) centered at the $\overline{\Gamma}$ point [blue and brown dashed parabolas in Figs. 3(a) and 3(c)]. The IP states are resonant with the bulk sp band at the $\overline{\Gamma}$ point, leading to their broadening and, therefore, weak signal strengths [68], but become surface states at larger parallel momenta $k_\parallel$, where they gain intensity because they enter the projected bandgaps.

In the following sections, we will elaborate on assignments of the observed transitions involving the surface states S1–S3, the image potential states IP1 and IP2, and the bulk bands B1–B4 in different orders of excitation.

B. S1: The partially occupied Shockley surface state

The Shockley surface state S1 is occupied in the range $k_{[001]} \sim 0.75 \pm 0.08$ Å^{-1}, from its band minimum at the $\overline{Y}$ point up to E_F. Therefore, it can act as an initial as well as an intermediate state in a nonlinear photoemission process, depending on the $k_{[001]}$ of detection. In Fig. 2(b), two-photon absorption lifts the electrons from the occupied range of the S1 state [S1$^{(occ)}$] to $E_f \sim 7.3$ eV. The effective mass of the band S1$^{(occ)} \sim 0.2$–$0.4\,m_e$ is consistent with its literature value of $0.26\,m_e$, as shown in Table I [46]. The unoccupied part of the S1 band [S1$^{(unocc)}$] also participates as an intermediate state in mPP processes when it is excited from the bulk sp-band continuum. This will be discussed further in conjunction with the 3PP and 4PP measurements.

TABLE I. Summary of the measured electronic band parameters from our experiments and comparison with the available literature values. The energies are given with respect to the Fermi level. The IP state binding energies are given with respect to the work function of ~4.25 eV.

	Experiment band minimum (eV)	Experiment band mass (m_e)	Literature band minimum (eV)	Literature band mass (m_e)
S1	−0.1	0.2–0.4	−0.1[a,b]	0.26[a]
S2	1.6	0.7	1.6,[b] 1.7[c]	0.9,[b] 0.7[c]
S3-$\overline{\Gamma X}$	7.4	–	1.75[d]	–
S3-$\overline{\Gamma Y}$	7.4	–	0.11[d]	–
IP1	−0.5	1.1–1.2	−0.15[b]	1.2[b]
IP2	−0.1	0.8	–	–

[a]Reference [46].
[b]Reference [47].
[c]Reference [48].
[d]Reference [44].

The S1 state is detected in the photoemission experiment only when electrons are excited above the photoemission horizon [compare blue arrows and green parabola in Fig. 1(b)]. Consequently, in the constant energy cuts through the 2PP spectra [Figs. 2(a) and 2(c)], it appears as concentric circles or circle arcs centered at the $\overline{Y}$ point (0.75 Å^{-1}). The abrupt constraint of the photoemission horizon allows S1$^{(occ)}$ to appear entirely as a complete circle, whereas S1$^{(unocc)}$ appears as an arc at $k_{[001]}$ at a larger distance from the $\overline{Y}$ point [Figs. 2(a) and 2(c)]. As the final state energy increases, the arc radii increase toward the $\overline{\Gamma}$ point.

Similar excitations as in 2PP also occur in higher order 3PP and 4PP processes with infrared-visible light. The S1$^{(occ)}$ state can be excited by absorbing 3 or 4 photons, labeled as S1$^{(occ)} + 3\hbar\omega$ and S1$^{(occ)} + 4\hbar\omega$ features at the $\overline{Y}$ point in Figs. 3(a) and 3(c). The 3PP and 4PP excitation of the S1$^{(occ)}$ state is discussed in detail in Ref. [51].

Once the S1 band crosses the Fermi level, the S1$^{(unocc)}$ state between the $\overline{Y}$ and $\overline{\Gamma}$ points can be populated through one-photon absorption and then be detected in 3PP and 4PP. Like the 2PP case, however, it requires absorption of two more photons to overcome the work function and thus is labeled as S1$^{(unocc)} + 2\hbar\omega$ in Figs. 3(a) and 3(c). Moreover, its corresponding above-threshold photoemission (ATP), where it is excited to above Φ and absorbs an extra one or more photons, S1$^{(unocc)} + 3\hbar\omega$, is observed in $\hbar\omega = 1.72$ eV excitation data [Fig. 3(c)] above the 3PP Fermi level edge signal. We mention here that a two-photon resonant transition from S1$^{(unocc)}$ to IP1 states resonantly enhances the S1$^{(unocc)} + 3\hbar\omega$ signal, as will be documented. Furthermore, the IP2 state can also come into a two-photon resonance with the S1$^{(unocc)}$ state, but the contribution of this process is considerably weaker such that it is not clear in the color scale display in Fig. 3(c). A similar excitation process is more evident from the S2 state, as we show next.

C. S2: The unoccupied Shockley surface state

Like the unoccupied part of the S1 state, the S2 state contributes to the 2PP signal only as an intermediate state at ~1.6 eV above E_F [Fig. 2(b)]; its recorded dispersion matches the literature value from scanning tunneling spectroscopy [48]. This is summarized in Table I. In Fig. 4(b), we plot the photon energy-dependent data of the S1 and S2

states from two-photon momentum microscopy. In agreement with an Einsteinian photoemission process, the slope of E_f with respect to the $\hbar\omega$ at a constant $k_\parallel$ depends on the number of photons needed to photoemit from the last real state that is populated in an mPP process instead of the total number of photons that excite it. Thus, the S1$^{(occ)}$ state, serving as an initial state, and the S1$^{(unocc)}$ and S2 states, serving as intermediate states in 2PP excitation, appear with slopes of 2.11, 1.35, and 1.15, respectively, as shown in Fig. 4(b). The deviations from integer slope values may indicate that other unknown states participate in the multiphoton process or simply reflect the uncertainties of determining the slopes from narrow spectral ranges.
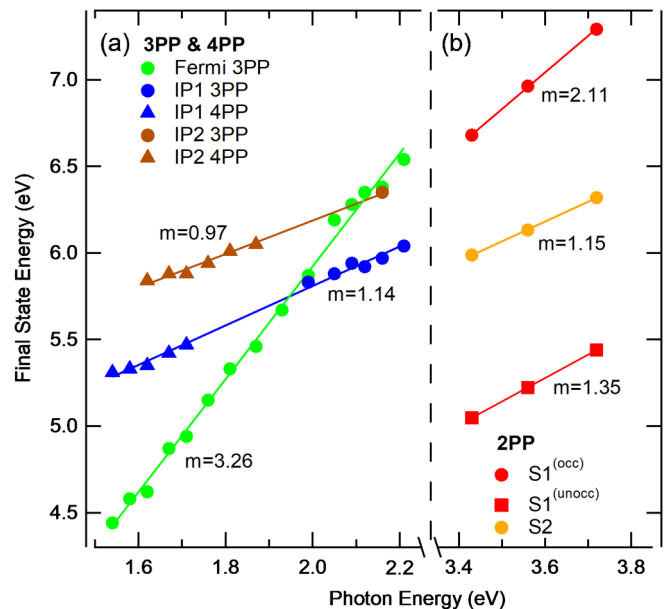

FIG. 4. Photon energy dependent E_f-energies of (a) the IP states and the Fermi level in 3PP and 4PP and (b) the surface states S1 and S2 in two-photon photoemission (2PP). 3PP and 4PP peak energies are extracted at $k_{[001]}=0$ Å^{-1} ($\overline{\Gamma}$ point). S1$^{(unocc)}$ and S2 energy positions are extracted at an intermediate momentum of $k_{[001]} = 0.37$ Å^{-1} while S1$^{(occ)}$ energy positions are extracted at the $\overline{Y}$ point ($k_{[001]} = 0.75$ Å^{-1}). The slope m values given in the figure approximately report the number of photons needed to photoemit electrons from specific states.

In the $\hbar\omega = 2.09$ eV 3PP excitation data [Fig. 3(a)], different momentum regions of the S2 state are excited with the same order 3PP process but involving different excitation pathways. For instance, the component of the S2 + $1\hbar\omega$ signal, which is located at a smaller $k_{[001]}$ and a higher energy is populated by two-photon absorption from the bulk sp band and detected by photoemission of one more photon, while in the case of the S2 + $2\hbar\omega$ signal, S2 is populated by one-photon absorption from the sp band followed by two-photon photoemission. The S2 + $1\hbar\omega$ 3PP signal is also observed in $\hbar\omega = 1.72$ eV excitation data [Fig. 3(c)], and at one-photon higher energy, the S2 + $2\hbar\omega$ feature appears once more as a four-photon ATP process where S2 is emitted by two photons. The two-photon excitation from S2 is enhanced when it involves resonant transitions to the IP states [81], but in this case, it does not involve ATP. For example, a one-photon resonant transition between IP1 and S2 states at $k_{[001]} \sim 0.3$ Å^{-1} enhances the signal intensity at the crossing point of blue and orange dashed parabolas in Fig. 3(c). Similar enhancement also occurs for the S2 and IP2 resonance but with lower intensity.

D. S3: The anisotropic surface state at the $\bar{\Gamma}$ point

Contrary to S1 and S2, the S3 state exists at the $\bar{\Gamma}$ point within a minigap in the final state energy region, with a highly anisotropic distribution that is derived from the real space anisotropy of the Ag(110) surface [44]. In Fig. 2(c), S3 appears as a bright, narrow rectangle. In the serrated $\overline{\Gamma Y}$ direction, the calculated band structure of the Ag(110) surface predicts the S3 band to be highly dispersive with a band mass of 0.11 m_e (Table I) [44]. The consequence of the strong dispersion is that it limits the S3 spectral density to a narrow $|k_{[001]}| < 0.05$ Å^{-1} region of high density of states (DOS) near its band minimum. In the smooth $\overline{\Gamma X}$ direction, however, it is much less dispersive with a calculated band mass of 1.75 m_e, which gives it a large DOS over a larger $k_{[1\bar{1}0]}$ range. Ergo, it appears as an elongated rectangle in the momentum microscope images in Fig. 2(c). DFT calculations in Fig. S1 in the Supplemental Material [80] of 2D DOS reproduce this unusual rectangular-shaped high DOS region at $E_f = 7.2$ eV, which confirms the highly anisotropic S3 state dispersions. Further orbital analysis shows that the S3 state has mainly contributions from the s and d atom-projected states (not shown). The charge density calculation also shows that the S3 state mostly locates in the first two atomic layers (Fig. S2 in the Supplemental Material [80]), and electrons occupying this state can either leave the surface or enter the bulk where there is also a small but finite density distribution. These characteristics show that the S3 state overlaps with the near-surface bulk bands.

As discussed in Sec. II, the spectroscopic brightness of the S3 state in 2PP spectra has been attributed to its participation as the final state in the non-Einsteinian plasmonic photoemission [44]. When the laser driving frequency exceeds the silver bulk plasmon frequency of 3.7–3.9 eV, the light penetrates as the bulk plasmon polarization, and annihilation of two bulk plasmon quanta excites photoelectrons specifically from E_F to populate the S3 state [43,44,73]. In addition to the plasmonic photoemission, S3 appears as a bright surface feature at the $\bar{\Gamma}$

point because, being within the projected bandgap above Φ, it couples to the resonant vacuum continuum into which it can decay without a barrier rather than to decay into the bulk, as do the much less bright bound IP resonances, to be discussed next.

E. IP1 and IP2: Image potential states

The IP states or resonances of Ag(110) have only been reported in IPE [47] but not in mPP experiments. In 2PP momentum microscopy data shown in Fig. 2, we do not observe spectroscopic signatures of these states, even though the excitation light in the $\hbar\omega = 3.43$–3.86 eV energy range is sufficiently energetic to excite them from the sp-bulk bands at the $\bar{\Gamma}$ point. By contrast, in Fig. 3, the IP states do appear as the penultimate intermediate states in the 3PP and 4PP processes, where their nearly free electron dispersions are represented by the blue and brown dashed parabolic lines in Figs. 3(a) and 3(c); the band minima at the $\bar{\Gamma}$ point, the free electronlike band masses, and the binding energies identify them as the IP1 and IP2 states (Table I) [82]. Note that the recorded IP state intensities are strongly momentum dependent and are particularly weak near the $\bar{\Gamma}$ point where they are resonances.

In Fig. 4(a), we plot the $\hbar\omega$-dependent E_f data of IP states detected in 3PP and 4PP spectra. In addition, we plot the 3PP Fermi level, which has a slope of 3.26 expected for an initial state in a 3PP process. By contrast, the IP1 and IP2 states appear with slopes of 1.14 and 0.97, as expected for the penultimate states in the excitation processes. The binding energies of IP1 and IP2 states relative to the vacuum level in Table I are comparatively small, suggesting that they have a large quantum defect on the (110) surface, which could arise from their interaction with the bulk [83].

As explained above, the resonance character of the IP states due to their interaction with the bulk sp band limits their participation in the 2PP excitation at the $\bar{\Gamma}$ point of Ag(110). Moreover, in 4PP measurements at the $\bar{\Gamma}$ point [Fig. 5(b)], the IP states hardly emerge from the continuous background, but their participation is confirmed by their dispersions. Therefore, in Fig. 5(a), the relatively strong IP state contrast at the $\bar{\Gamma}$ point in 3PP measurements is surprising.

Additional photon energy-dependent data at the $\bar{\Gamma}$ point in Fig. 5(c) show that for $\gtrsim 2$ eV photon energy, the 3PP Fermi level signal is abnormally elevated, forming a peaklike structure instead of an expected shoulder, representing the occupied Fermi-Dirac DOS that is commonly observed in photoemission spectra of metals [84]. Above 2 eV excitation, this elevated signal evolves into a separate shoulderlike Fermi level and a peak which we attribute to the IP1 state. This structure may be interpreted as an enhanced Fermi level excitation promoting 3PP by two-photon excitation via the IP state. Note also that the $\hbar\omega = 1.9$ eV excitation is special for silver because it is not only $\frac{1}{2}$ of the bulk plasmon frequency, and as such could enhance nonlinear processes, but it also corresponds to the energy where the transient exciton feature appears in the two-photon resonant Shockley state to the IP1 state transition on Ag(111) [14,16,41]. We note that there is no surface or bulk band structure in the single-particle Ag(110) spectra that could explain the intensification of the Fermi
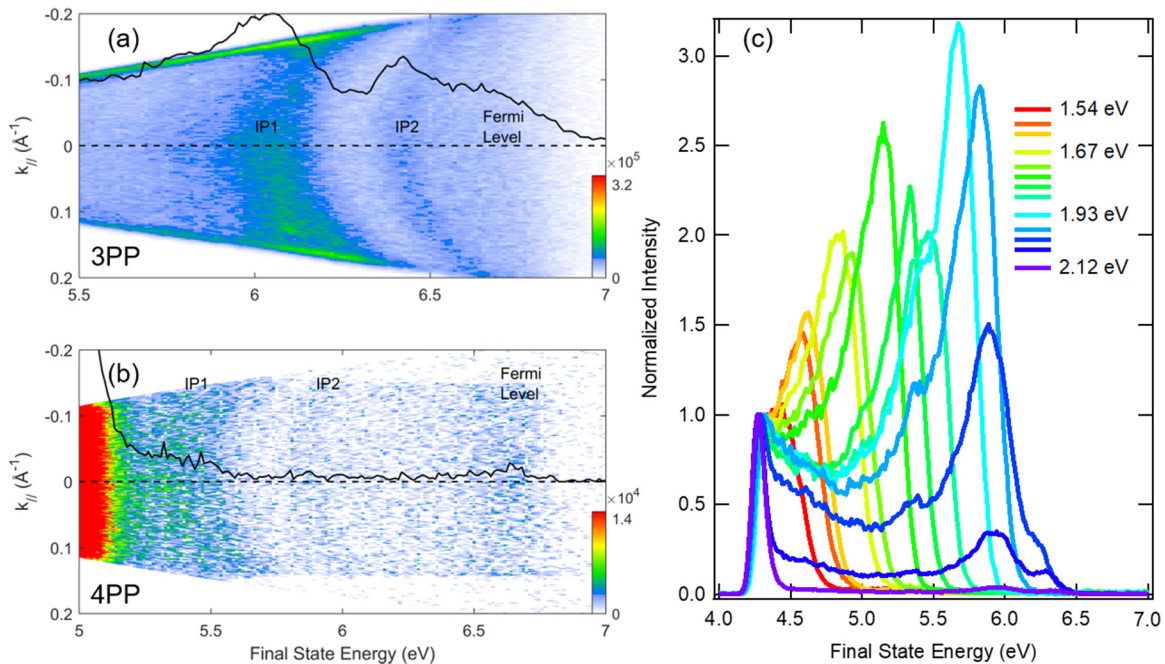
FIG. 5. IP states excitation of Ag(110) data at $\bar{\Gamma}$ point when sample $\overline{\Gamma X}$ direction is in the optical plane. The $E_f(k_{[1\bar{1}0]})$ spectra are collected for (a) 2.28 eV and (b) 1.67 eV photon energies, and the IP states are detected in three-photon photoemission (3PP) and four-photon photoemission (4PP), respectively. The black solid line represents a line profile taken at the $\bar{\Gamma}$ point. IP1 and IP2 states and E_F level signals are visible. (c) Photon energy-dependent energy line profiles taken at the $\bar{\Gamma}$ point. An elevated E_F level signal develops into the IP1 state and shoulder-shaped Fermi level when $\hbar\omega$ is tuned through 1.9 eV. Note that the intensities are normalized at the work function edge, which suppresses the E_F edge amplitude for the highest $\hbar\omega$ data because the work function edge signal is enhanced by onset of the signal from two-photon photoemission (2PP). The data are taken with the sample aligned in the $\overline{\Gamma X}$ direction to eliminate the contributions from other surface states; otherwise, the spectra have the same appearance.

edge. The reason for the enhancement of the E_F edge in 3PP requires further scrutiny. Nevertheless, we speculate that these circumstances enhance the visibility of the IP states in 3PP over 2PP and 4PP.

Apart from the nonlinear order intensity differences, the IP state signal intensifies as $k_{[001]}$ moves from a resonance at the $\bar{\Gamma}$ point to a surface state within the projected bandgap in the $\overline{\Gamma Y}$ direction; this is evident in 3PP and 4PP spectra in Fig. 3(a), where the IP1 state signal is enhanced between $k_{[001]} \sim 0.2$ and $0.4\,\text{Å}^{-1}$. In addition to the role of the bandgap, this intensity enhancement can also be attributed to resonant transitions from the S1/S2 surface states to IP states. For instance, the IP1 state appears with high intensity at the crossing with the S2 + $2\hbar\omega$ signal where it participates in a one-photon resonant transition from the S2 band, as already discussed. Moreover, at larger $k_{[001]}$, the two-photon resonant IP1 ← S1$^{(\text{unocc})}$ transition can also enhance the signal. The IP2 has similar resonances but with less intensity, probably because of a smaller wave function overlap.

F. B1–B4: *sp*-bulk band transitions

After accounting for the known surface states, the remaining photoemission spectral features in the 2PP momentum microscopy data in Fig. 2 must involve transitions from the occupied to the unoccupied *sp* bands. Such transitions have been extensively studied for the (111)-oriented Ag surface [12,15,23,43,85], where below the bulk plasmon frequency, they are promoted by the dynamical multipole plasmon

screening response of silver; they, however, have not been investigated for the (110) crystal orientation [44,49,86].

To define where the bulk band transitions may occur, we make use of the calculated $k_\perp$ bulk band structures by plotting E-E_F vs $k_{||}$ dispersions at equidistant $k_\perp$ points along the bulk ΓK direction. The relevant bulk band structure profiles at three different $k_\perp = 0.82$, 0.93, and $0.77\,\text{Å}^{-1}$ regions are plotted separately in Figs. 6(a)–6(c), where the B3, B1, and B2 excitations in 2PP are assigned to the respective B ← A, D ← A, and C ← A transitions in the following. These transitions are also excited with *s*-polarized light (not shown), according to the optical transition moments.

The B1 band [Fig. 6(b)], whose dispersion is shown for the $\overline{\Gamma Y}$ direction, involves a one-photon transition from band A to band D and appears over the photon energy ranging from $\hbar\omega = 2.83$ to $> 4.15\,\text{eV}$ (not shown). Varying the excitation energy defines different $k_\perp$ and $k_{||}$ in B1 that satisfy the energy and parallel momentum conservation in resonant optical transitions. Due to the different $k_{||}$ dispersions of bands A and D, the resonant transitions between them are excited over a limited energy range ($\sim 1\,\text{eV}$).

The B3 band [Fig. 6(a)] in the $\overline{\Gamma X}$ direction involves a similar excitation mechanism but disappears for the $\hbar\omega < 3.5\,\text{eV}$ excitation because of a larger gap between bands A and B, which shows good agreement between the experiment and theory.

The B2 band [Fig. 6(c)], involving a two-photon resonant transition between bands A and C near the $\bar{Y}$ point, corresponds to the well-known two-photon transition between
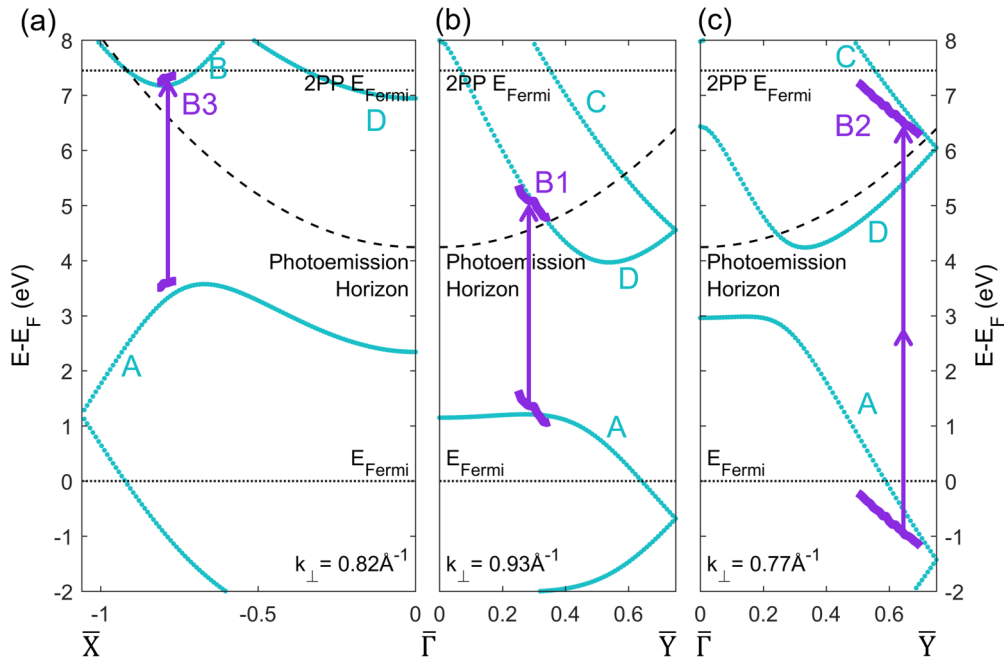
FIG. 6. Bulk band transition assignments from two-photon photoemission (2PP) spectroscopy plotted relative to the calculated Ag(110) $k_\perp$ bulk band structures. (a)–(c) $\overline{\Gamma X}$ and $\overline{\Gamma Y}$ cuts for selected $k_\perp$ momenta along the bulk ΓK direction. The calculated sp-bulk bands are labeled with uppercase letters (A–D). The spectroscopic features B1–B3 identified in Fig. 2 are plotted as solid purple lines. The features B1 and B3 can be attributed to one-photon bulk transitions. The feature B2 is a two-photon sp-bulk transition.

the lower and upper sp bands of Ag(111) that is centered at the $\bar{\Gamma}$ point [15,43]; on the (110) surface, however, it is observed normal to the (111) planes that form it. Although the sp-band signal appears for excitations ranging between 2.6 and 3.9 eV for Ag(111) [43,44], the B2 band on Ag(110) disappears below $\hbar\omega = 3$ eV excitation at large $k_{||}$ because it is cut off by the photoemission horizon. A common feature of both surfaces is that the bulk 2PP signals disappear for $\hbar\omega > 3.9$ eV excitation, although the transition is allowed from a pure band structure perspective, as shown in Fig. 2 of Ref. [43]. We attribute the vanishing of the B2 signal to the frequency-dependent dynamical screening of the surface fields [1,44,86], which defines the near-surface field strengths that drive the nonlinear process. The 2PP process being proportional to $E(\omega)^4$ is strongly dependent on such multipole plasmon response of Ag, which becomes ineffective above the bulk plasmon frequency of $\sim$3.9 eV [43,45,87–89]. Moreover, this C ← A bulk band transition can also be excited by three- and four-photon resonance with a weaker intensity because the resonant transition involves the unoccupied part of band A, which must be populated first by absorbing an additional photon (Fig. S3 in the Supplemental Material [80]).

We note that transitions between the initial and final bulk bands can occur between states of different $k_\perp$, which is not conserved in photoemission. Our analysis, however, which considers fixed $k_\perp$ for resonant transitions, already gives a good match with experiments. The matching could be improved by considering the 3D bulk band structure, but because the calculated electronic band structures are not exact, this is unlikely to generate more accurate assignments.

Finally, there is a very weak feature B4 in Figs. 2(a) and 2(c) which we assign to a one-photon photoemission from the upper sp-bandgap edge of Ag(110) about the $\bar{Y}$ point, which

must be populated from the lower sp band. The photon energy is insufficient for one-photon excitation, so such a transition must involve either a two-photon excitation or promotion of hot electrons from above E_F. The detection of electrons in the upper sp band has been previously proposed [90], and it also occurs weakly in 2PP spectra of Ag(111) at the $\bar{\Gamma}$ point. There, an additional dispersive feature clearly separates from that of the IP1 state at parallel momentum $k_{||} \sim 0.15$ Å^{-1} above the IP state in Fig. 1(e) of Ref. [43]; this feature, however, is not the focus of this paper.

Although we attribute these features to the bulk bands, we note that their appearance is promoted by a strong surface character arising from several factors. Because light cannot penetrate deeply, and more pertinently, because the multipole plasmon response screens its penetration by generating intense surface local fields for excitation below the bulk plasmon frequency [89,91,92], the bulk bands that have large transition moments also must have a large near-surface density [12].

V. DISCUSSION

So far, we have described and assigned the 3D nonlinear photoemission momentum microscope energy-$k_{||}$ images of anisotropic electronic bands of the Ag(110) surface. Specifically, we have identified three surface states (S1–S3), the first and the second image potential states (IP1 and IP2), as well as four bulk interband transitions (B1–B4). Our results, i.e., the surface state binding energies and their effective masses are summarized and compared with the experimental and related literature values in Table I. In addition, all the band dispersions are plotted in Fig. 7 as thick solid lines at energies where they appear in 2PP spectra as the initial,
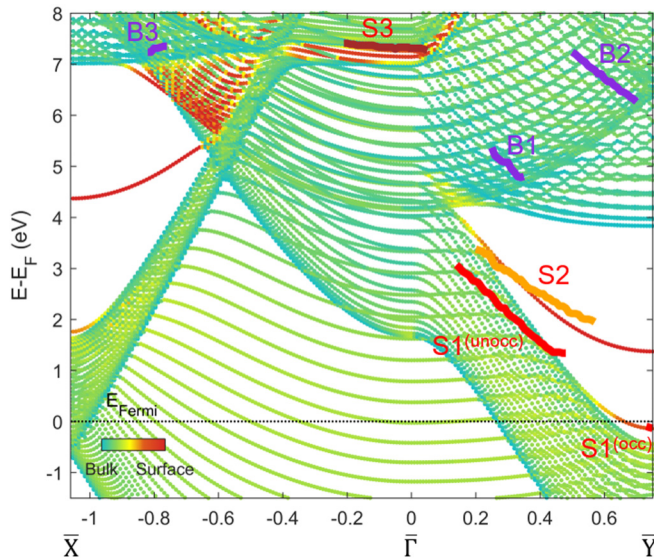
FIG. 7. Summary of the experimental results and comparison with the calculated surface and bulk band structures of Ag(110) surface in the $\overline{\Gamma X}$ [1$\overline{1}$0] and $\overline{\Gamma Y}$ [001] directions. The color scale shows their relative surface character. State dispersions (S1–S3, B1–B3) are extracted from momentum microscope data in Fig. 2. S1$^{(unocc)}$ and S1$^{(occ)}$ (red line) represent the excitation from the unoccupied and occupied part of the S1 state, respectively. S2 (orange line) represents unoccupied S2 state excitation. S3 (brown line) is a highly anisotropic S3 surface state at $\overline{\Gamma}$ point. States B1–B3 (purple lines) represent bulk band excitations.

intermediate, or final states, giving a comprehensive understanding of the possible electronic transitions taking place at the pristine Ag(110) surface. Our results are consistent with the calculated electronic band structure and explain the discovery of the unexpected wealth of dispersive features in the 3D momentum microscope spectra in Fig. 2. In the following, we further discuss our results (i) in comparison with the Cu(110) surface, (ii) implications of using higher-order photoemission spectroscopy for mapping complex band structures, and (iii) the general prospect of multiphoton momentum microscopy to study the nonlinear response of metal surfaces in the energy-momentum space.

As already noted, the nonlinear response of the Cu(110) surface has been investigated by 2PP with UV excitation light [52]. The Cu(110) surface also has surprisingly rich spectral features primarily involving transitions from the copper d bands starting at 2 eV below E_F through the intermediate lower sp band, and terminating in final states associated with the upper sp band near the $\overline{\Gamma}$ point [52]. Because the d bands of silver lie deeper in the band structure (∼4 eV below E_F), they make no contribution to the Ag(110) mPP spectra that we have recorded and assigned. Consequently, on Ag(110), the occupied S1 band is the dominant initial state in a narrow $k_\parallel$ range around the $\overline{Y}$ point, and elsewhere, the mPP process must initiate from the occupied bulk sp band. Because of the strong 3D dispersion of this bulk band and lack of $k_\perp$ conservation, it is difficult to attribute specific regions of the sp band that are particularly spectroscopically active under

our experimental conditions. One should recall that the strong bulk band contribution in mPP spectra of Ag(110) derives from the local field enhancement by the multipole plasmon response [1,43,88,89]. The multipole plasmon enhances the fields in the near-surface region giving the observed spectra strong surface character in the sense that the surface and bulk bands are optically coupled.

We have employed photon energies ranging from infrared to UV to excite electrons above the work function, and in some cases above the threshold, in the nonlinear orders of $m = 2, 3$, and 4. The excitation may be considered as either multiphoton absorption via intermediate resonances or Floquet engineering of the electronic bands [21,24,51]. Depending on the photon energy, we are distinctly sensitive to different dipole transitions in the photoexcitation process. This is most evident in our ability to resolve the IP states prominently in 3PP, whereas they are dark in 2PP even though the bulk sp bands can act as initial states for their population in either case. We surmise that this happens because of distinct resonances that potentially enhance the photoexcitation process, but such an interpretation requires further scrutiny. Thus, to obtain a more comprehensive band mapping of a complex electronic structure, we propose that it can indeed be helpful to investigate the electronic bands of a solid in multiple nonlinear orders in the perturbative regime.

Finally, we note that our results showcase the strength of two-photon momentum microscopy experiments. This has already been established in several selected examples [28,30,93], particularly for investigation of exciton structure and dynamics in 2D materials [26,94]. Our data, however, notably make it evident that this approach is especially well suited for anisotropic surfaces. The full anisotropic electronic band structure and all the (non)linear optical transitions that occur within it can be accessed simultaneously without concern on how the incidence of light affects its interaction with a solid. In the case of the Ag(110) surface, this is especially advantageous because it is not necessary to consider how the measurements depend on the relative electric field polarization through the field polarization and sample-orientation dependence of dipole matrix elements. Such effects play a significant role in photoemission involving the S2 ← S1$^{(occ)}$ resonance on Ag(110) [29,41,51]. One can also envision that, because momentum microscope measurements provide information on the real space distribution of the electronic wave functions [34,37,95] and their electron dynamics [96], one may be able to achieve similar real space resolved imaging of electronic bands and their dynamics.

VI. CONCLUSIONS

In conclusion, we have measured energy and momentum-resolved 2PP–4PP spectra with $\hbar\omega = 1.33$–4.15 eV from the pristine Ag(110) surface by multidimensional momentum microscopy and angle-resolved mPP spectroscopy techniques. The multiphoton excitation enables probing of optical processes within the energetically accessible parts of the Brillouin zone, without a requirement for high-energy UV photons [25,51]. The combination of momentum imaging and direct access to the coherent response of solids [24] opens the way to image the electronic wave functions of

the coupled bands [34,37,95] and to record the dressing of electronic bands in the energy-momentum space [21,29]. We identified the participation of two Shockley surface states centered at the $\bar{Y}$ point as the initial and intermediate states in mPP excitation processes that can be excited through different pathways in different order excitations, enabling their spectroscopic characterization over a much broader energy-momentum range than can be accomplished by linear optical excitation. These surface states are distributed with strong anisotropy in real space and $k_{||}$, yet they are isotropic about the $\bar{Y}$ points. We have also identified a surface state within a minibandgap, which is strongly anisotropic around the $\bar{\Gamma}$ point in the momentum space and acts as a final state for the plasmonically induced emission in 2PP. Other states that can be effectively populated include the first and the second image potential states as well as several regions of the bulk sp bands. Our momentum imaging capability reveals the IP state responses, which are weak at the $\bar{\Gamma}$ point where they are resonances and become stronger as they emerge into surface projected bandgaps centered at the $\bar{Y}$ points. We emphasize that mPP processes at metal surfaces have revealed a rich complement of optical phenomena that are usually not considered in the linear photoelectron spectroscopy, such as interband optical transitions [97], spin polarization of electronic bands [98], plasmonic field-mediated single-particle excitations [43,44], transient exciton responses [16], and Floquet engineering and optical dressing of electronic transitions in mPP [21,24,29,99].

Our research results present a comprehensive study of the nonlinear photoemission spectra as obtained on the pristine Ag(110) surface. The detailed understanding of the surface and bulk electronic bands is essential for the subsequent study of adsorbates on these surfaces that potentially hybridize with the surface states or are excited by coherent charge transfer excitation [100]. The strong coupling between the molecules and metallic surface states has been documented for Ag(111) and Ag(100) surfaces by two-photon photoemission spectroscopy and theory [101,102]. The atomic-scale corrugation and the spatial and momentum displacement of the two Shockley surface states on Ag(110) presents challenges and opens possibilities for investigations of the coupled light-matter and/or adsorbate-substrate interactions. Last but not least, the plasmonically driven hot electron excitation process that occurs on all three low-index Ag surfaces [44] can reveal how specific excitations play a role in energy harvesting processes [103,104].

[1] P. Feibelman, Prog. Surf. Sci. **12**, 287 (1982).

[2] P. M. Echenique, R. Berndt, E. V. Chulkov, T. Fauster, A. Goldmann, and U. Höfer, Surf. Sci. Rep. **52**, 219 (2004).

[3] F. Reinert, G. Nicolay, S. Schmidt, D. Ehm, and S. Hüfner, Phys. Rev. B **63**, 115415 (2001).

[4] M. Bauer, A. Marienfeld, and M. Aeschlimann, Prog. Surf. Sci. **90**, 319 (2015).

[5] H. Petek and S. Ogawa, Prog. Surf. Sci. **56**, 239 (1997).

[6] W. L. Chan, M. Ligges, A. Jailaubekov, L. Kaake, L. Miaja-Avila, and X. Y. Zhu, Science **334**, 1541 (2011).

[7] F. S. Tautz, Prog. Surf. Sci. **82**, 479 (2007).

[8] C. Zhan, X.-J. Chen, J. Yi, J.-F. Li, D.-Y. Wu, and Z.-Q. Tian, Nat. Rev. Chem. **2**, 216 (2018).

[9] U. Aslam, V. G. Rao, S. Chavez, and S. Linic, Nat. Catal. **1**, 656 (2018).

[10] P. V. Kamat and G. V. Hartland, ACS Energy Lett. **3**, 1467 (2018).

[11] E. D. Hansen, T. Miller, and T. C. Chiang, Phys. Rev. B **55**, 1871 (1997).

[12] T. Miller, E. D. Hansen, W. E. McMahon, and T. C. Chiang, Surf. Sci. **376**, 32 (1997).

[13] V. M. Silkin, P. Lazić, N. Došlić, H. Petek, and B. Gumhalter, Phys. Rev. B **92**, 155405 (2015).

[14] C. M. Li, L. E. Urbach, and H. L. Dai, Phys. Rev. B **49**, 2104 (1994).

[15] A. Winkelmann, V. Sametoglu, J. Zhao, A. Kubo, and H. Petek, Phys. Rev. B **76**, 195428 (2007).

[16] X. Cui, C. Wang, A. Argondizzo, S. Garrett-Roe, B. Gumhalter, and H. Petek, Nat. Phys. **10**, 505 (2014).

[17] S. Ogawa, H. Nagano, H. Petek, and A. P. Heberle, Phys. Rev. Lett. **78**, 1339 (1997).

[18] U. Höfer, I. L. Shumay, C. Reuß, U. Thomann, W. Wallauer, and T. Fauster, Science **277**, 1480 (1997).

[19] T. Hertel, E. Knoesel, M. Wolf, and G. Ertl, Phys. Rev. Lett. **76**, 535 (1996).

[20] A. Winkelmann, F. Bisio, R. Ocana, W. C. Lin, M. Nyvlt, H. Petek, and J. Kirschner, Phys. Rev. Lett. **98**, 226601 (2007).

[21] M. Reutzel, A. Li, Z. Wang, and H. Petek, Nat. Commun. **11**, 2230 (2020).

[22] R. Arafune, N. Takagi, and H. Ishida, Prog. Surf. Sci. **93**, 177 (2018).

[23] N. Pontius, V. Sametoglu, and H. Petek, Phys. Rev. B **72**, 115105 (2005).

[24] M. Reutzel, A. Li, and H. Petek, Phys. Rev. X **9**, 011044 (2019).

[25] M. Reutzel, A. Li, and H. Petek, Phys. Rev. B **101**, 075409 (2020).

[26] J. A. Sobota, Y. He, and Z.-X. Shen, Rev. Mod. Phys. **93**, 025006 (2021).

[27] A. Winkelmann, C. Tusche, A. A. Ünal, C.-T. Chiang, A. Kubo, L. Wang, and H. Petek, in *Solar Energy Conversion: Dynamics of Interfacial Electron and Excitation Transfer*, edited by P. Piotrowiak (The Royal Society of Chemistry, Cambridge, 2013), p. 225.

[28] A. A. Ünal, C. Tusche, S. Ouazi, S. Wedekind, C.-T. Chiang, A. Winkelmann, D. Sander, J. Henk, and J. Kirschner, Phys. Rev. B **84**, 073107 (2011).

[29] M. Keunecke, M. Reutzel, D. Schmitt, A. Osterkorn, T. A. Mishra, C. Möller, W. Bennecke, G. S. Matthijs Jansen, D. Steil, S. R. Manmana, S. Steil, S. Kehrein, and S. Mathias, Phys. Rev. B **102**, 161403(R) (2020).

[30] F. Haag, T. Eul, P. Thielen, N. Haag, B. Stadtmüller, and M. Aeschlimann, Rev. Sci. Instrum. **90**, 103104 (2019).

[31] C. Tusche, A. Krasyuk, and J. Kirschner, Ultramicroscopy **159**, 520 (2015).

[32] W. L. Mochán, R. G. Barrera, Y. Borensztein, and A. Tadjeddine, Physica A **207**, 334 (1994).

[33] J. Xu, X. Zhu, S. Tan, Y. Zhang, B. Li, Y. Tian, H. Shan, X. Cui, A. Zhao, Z. Dong, J. Yang, Y. Luo, B. Wang, and J. G. Hou, Science **371**, 818 (2021).

[34] P. Puschnig, S. Berkebile, A. J. Fleming, G. Koller, K. Emtsev, T. Seyller, J. D. Riley, C. Ambrosch-Draxl, F. P. Netzer, and M. G. Ramsey, Science **326**, 702 (2009).

[35] C. Leandri, G. L. Lay, B. Aufray, C. Girardeaux, J. Avila, M. E. Dávila, M. C. Asensio, C. Ottaviani, and A. Cricenti, Surf. Sci. **574**, L9 (2005).

[36] M. Ohta, K. Watanabe, and Y. Matsumoto, J. Phys. Chem. B **105**, 8170 (2001).

[37] G. S. M. Jansen, M. Keunecke, M. Düvel, C. Möller, D. Schmitt, W. Bennecke, F. J. S. Kappert, D. Steil, D. R. Luke, S. Steil, and S. Mathias, New J. Phys. **22**, 063012 (2020).

[38] D. S. Martin, N. P. Blanchard, P. Weightman, D. S. Roseburgh, R. J. Cole, J. K. Hansen, J. Bremer, and O. Hunderi, Phys. Rev. B **76**, 115403 (2007).

[39] Y. Borensztein, W. L. Mochan, J. Tarriba, R. G. Barrera, and A. Tadjeddine, Phys. Rev. Lett. **71**, 2334 (1993).

[40] T. Farrell, P. Harrison, C. I. Smith, D. S. Martin, and P. Weightman, Appl. Phys. Lett. **93**, 191102 (2008).

[41] L. E. Urbach, K. L. Percival, J. M. Hicks, E. W. Plummer, and H. L. Dai, Phys. Rev. B **45**, 3769 (1992).

[42] S. R. Barman, C. Biswas, and K. Horn, Surf. Sci. **566-568**, 538 (2004).

[43] M. Reutzel, A. Li, B. Gumhalter, and H. Petek, Phys. Rev. Lett. **123**, 017404 (2019).

[44] A. Li, M. Reutzel, Z. Wang, D. Novko, B. Gumhalter, and H. Petek, ACS Photonics **8**, 247 (2021).

[45] D. Novko, V. Despoja, M. Reutzel, A. Li, H. Petek, and B. Gumhalter, Phys. Rev. B **103**, 205401 (2021).

[46] A. Gerlach, G. Meister, R. Matzdorf, and A. Goldmann, Surf. Sci. **443**, 221 (1999).

[47] W. Altmann, V. Dose, and A. Goldmann, Z. Physik B - Condensed Matter **65**, 171 (1986).

[48] J. I. Pascual, Z. Song, J. J. Jackiw, K. Horn, and H. P. Rust, Phys. Rev. B **63**, 241103(R) (2001).

[49] T. Eul, J. Braun, B. Stadtmuller, H. Ebert, and M. Aeschlimann, Phys. Rev. Lett. **127**, 196405 (2021).

[50] N. F. Kleimeier, G. Wenzel, A. J. Urban, M. R. Tchalala, H. Oughaddou, Y. Dedkov, E. Voloshina, and H. Zacharias, Phys. Chem. Chem. Phys. **21**, 17811 (2019).

[51] A. Li, N. A. James, T. Wang, Z. Wang, H. Petek, and M. Reutzel, New J. Phys. **22**, 073035 (2020).

[52] Y. Sonoda, Phys. Rev. B **83**, 245410 (2011).

[53] S. S. Tsirkin, S. V. Eremeev, and E. V. Chulkov, Phys. Solid State **52**, 188 (2010).

[54] S. S. Tsirkin and E. V. Chulkov, J. Exp. Theor. Phys. **118**, 167 (2014).

[55] S. V. Eremeev, S. S. Tsirkin, and E. V. Chulkov, Phys. Rev. B **82**, 035424 (2010).

[56] S. S. Tsirkin, S. V. Eremeev, and E. V. Chulkov, Phys. Rev. B **84**, 115451 (2011).

[57] I. Y. Sklyadneva, R. Heid, K.-P. Bohnen, and E. V. Chulkov, in *Rufus Ritchie, A Gentleman and A Scholar*, edited by J. R. Sabin and J. Oddershede (Academic Press, Cambridge, MA, 2019), p. 199.

[58] K. Medjanik, O. Fedchenko, S. Chernov, D. Kutnyakhov, M. Ellguth, A. Oelsner, B. Schönhense, T. R. F. Peixoto, P. Lutz, C.-H. Min, F. Reinert, S. Däster, Y. Acremann, J. Viefhaus, W. Wurth, H. J. Elmers, and G. Schönhense, Nat. Mater. **16**, 615 (2017).

[59] M. Keunecke, C. Möller, D. Schmitt, H. Nolte, G. S. Matthijs Jansen, M. Reutzel, M. Gutberlet, G. Halasi, D. Steil, S. Steil, and S. Mathias, Rev. Sci. Instrum. **91**, 063905 (2020).

[60] C. Lin, K. Ikeda, Y. Shiota, K. Yoshizawa, and T. Kumagai, J. Chem. Phys. **151**, 144705 (2019).

[61] M. Hartelt, P. N. Terekhin, T. Eul, A.-K. Mahro, B. Frisch, E. Prinz, B. Rethfeld, B. Stadtmüller, and M. Aeschlimann, ACS Nano **15**, 19559 (2021).

[62] A. Winkelmann, A. Akin Ünal, C. Tusche, M. Ellguth, C.-T. Chiang, and J. Kirschner, New J. Phys. **14**, 083027 (2012).

[63] K. Giesen, F. Hage, F. J. Himpsel, H. J. Riess, and W. Steinmann, Phys. Rev. Lett. **55**, 300 (1985).

[64] S. Garrett-Roe, S. T. Shipman, P. Szymanski, M. L. Strader, A. Yang, and C. B. Harris, J. Phys. Chem. B **109**, 20370 (2005).

[65] M. Marks, C. H. Schwalb, K. Schubert, J. Güdde, and U. Höfer, Phys. Rev. B **84**, 245402 (2011).

[66] T. Fauster, M. Weinelt, and U. Höfer, Prog. Surf. Sci. **82**, 224 (2007).

[67] L. Vitali, P. Wahl, M. A. Schneider, K. Kern, V. M. Silkin, E. V. Chulkov, and P. M. Echenique, Surf. Sci. **523**, L47 (2003).

[68] U. Höfer and P. M. Echenique, Surf. Sci. **643**, 203 (2016).

[69] R. Rosei, C. H. Culp, and J. H. Weaver, Phys. Rev. B **10**, 484 (1974).

[70] E. Knoesel, A. Hotzel, T. Hertel, M. Wolf, and G. Ertl, Surf. Sci. **368**, 76 (1996).

[71] M. L. Brongersma, N. J. Halas, and P. Nordlander, Nat. Nanotechnol. **10**, 25 (2015).

[72] A. M. Brown, R. Sundararaman, P. Narang, W. A. Goddard, and H. A. Atwater, ACS Nano **10**, 957 (2016).

[73] J. J. Hopfield, Phys. Rev. **139**, A419 (1965).

[74] J. Kröger, M. Becker, H. Jensen, Th. von Hofe, N. Néel, L. Limot, R. Berndt, S. Crampin, E. Pehlke, C. Corriol,

V. M. Silkin, D. Sánchez-Portal, A. Arnau, E. V. Chulkov, and P. M. Echenique, Prog. Surf. Sci. **82**, 293 (2007).

[75] J. Maklar, S. Dong, S. Beaulieu, T. Pincelli, M. Dendzik, Y. W. Windsor, R. P. Xian, M. Wolf, R. Ernstorfer, and L. Rettig, Rev. Sci. Instrum. **91**, 123112 (2020).

[76] B. Kromker, M. Escher, D. Funnemann, D. Hartung, H. Engelhard, and J. Kirschner, Rev. Sci. Instrum. **79**, 053702 (2008).

[77] P. Giannozzi, S. Baroni, N. Bonini, M. Calandra, R. Car, C. Cavazzoni, D. Ceresoli, G. L. Chiarotti, M. Cococcioni, I. Dabo, A. Dal Corso, S. de Gironcoli, S. Fabris, G. Fratesi, R. Gebauer, U. Gerstmann, C. Gougoussis, A. Kokalj, M. Lazzeri, L. Martin-Samos *et al.*, J. Phys. Condens. Matter **21**, 395502 (2009).

[78] D. R. Hamann, Phys. Rev. B **88**, 085117 (2013).

[79] J. P. Perdew, K. Burke, and M. Ernzerhof, Phys. Rev. Lett. **77**, 3865 (1996).

[80] See Supplemental Material at http://link.aps.org/supplemental/10.1103/PhysRevB.105.075105 for a movie of the 3D 2PP momentum microscopy data, 2D DOS and spatial charge density distribution calculations of the S3 state, and the C ← A bulk band transition excited with different numbers of photons.

[81] F. Bisio, M. Nyvlt, J. Franta, H. Petek, and J. Kirschner, Phys. Rev. Lett. **96**, 087601 (2006).

[82] T. Fauster and W. Steinmann, in *Photonic Probes of Surfaces*, edited by P. Halevi (Elsevier, Amsterdam, 1995), p. 347.

[83] M. Weinelt, J. Phys. Condens. Matter **14**, R1099 (2002).

[84] S. Ogawa and H. Petek, Surf. Sci. **363**, 313 (1996).

[85] T. Miller, W. E. McMahon, and T. C. Chiang, Phys. Rev. Lett. **77**, 1167 (1996).

[86] K. J. Song, D. Heskett, H. L. Dai, A. Liebsch, and E. W. Plummer, Phys. Rev. Lett. **61**, 1380 (1988).

[87] J. M. Pitarke, V. M. Silkin, E. V. Chulkov, and P. M. Echenique, Rep. Prog. Phys. **70**, 1 (2007).

[88] K.-D. Tsuei, E. W. Plummer, A. Liebsch, K. Kempa, and P. Bakshi, Phys. Rev. Lett. **64**, 44 (1990).

[89] M. Rocca, in *Springer Handbook of Surface Science*, edited by M. Rocca, T. S. Rahman, and L. Vattuone (Springer International Publishing, Cham, 2020), p. 531.

[90] F. Bisio, A. Winkelmann, C. T. Chiang, H. Petek, and J. Kirschner, J. Phys. Condens. Matter **23**, 485002 (2011).

[91] A. Liebsch, Phys. Rev. B **36**, 7378 (1987).

[92] M. Merschdorf, C. Kennerknecht, and W. Pfeiffer, Phys. Rev. B **70**, 193401 (2004).

[93] F. Haag, T. Eul, L. Grad, N. Haag, J. Knippertz, S. Mathias, M. Cinchetti, M. Aeschlimann, and B. Stadtmüller, Phys. Rev. B **104**, 104308 (2021).

[94] R. Wallauer, P. Marauhn, J. Reimann, S. Zoerb, F. Kraus, J. Güdde, M. Rohlfing, and U. Höfer, Phys. Rev. B **102**, 125417 (2020).

[95] S. Weiss, D. Lüftner, T. Ules, E. M. Reinisch, H. Kaser, A. Gottwald, M. Richter, S. Soubatch, G. Koller, M. G. Ramsey, F. S. Tautz, and P. Puschnig, Nat. Commun. **6**, 8287 (2015).

[96] R. Wallauer, M. Raths, K. Stallberg, L. Münster, D. Brandstetter, X. Yang, J. Güdde, P. Puschnig, S. Soubatch, C. Kumpf, F. C. Bocquet, F. S. Tautz, and U. Höfer, Science **371**, 1056 (2021).

[97] A. Winkelmann, W.-C. Lin, C.-T. Chiang, F. Bisio, H. Petek, and J. Kirschner, Phys. Rev. B **80**, 155128 (2009).

[98] A. Winkelmann, W. C. Lin, F. Bisio, H. Petek, and J. Kirschner, Phys. Rev. Lett. **100**, 206601 (2008).

[99] F. Sirotti, N. Beaulieu, A. Bendounan, M. G. Silly, C. Chauvet, G. Malinowski, G. Fratesi, V. Véniard, and G. Onida, Phys. Rev. B **90**, 035401 (2014).

[100] H. Petek, J. Chem. Phys. **137**, 091704 (2012).

[101] C. H. Schwalb, S. Sachs, M. Marks, A. Scholl, F. Reinert, E. Umbach, and U. Hofer, Phys. Rev. Lett. **101**, 146801 (2008).

[102] S. S. Tsirkin, N. L. Zaitsev, I. A. Nechaev, R. Tonner, U. Höfer, and E. V. Chulkov, Phys. Rev. B **92**, 235434 (2015).

[103] L. Brus, Acc. Chem. Res. **41**, 1742 (2008).

[104] B. Seemala, A. J. Therrien, M. Lou, K. Li, J. P. Finzel, J. Qi, P. Nordlander, and P. Christopher, ACS Energy Lett. **4**, 1803 (2019).